# Nonequilibrium inelastic electronic transport: Polarization effects and vertex corrections to the self-consistent Born approximation

L. K. Dash,* H. Ness, and R. W. Godby
*Department of Physics, University of York, Heslington, York YO10 5DD, United Kingdom and European Theoretical Spectroscopy Facility (ETSF)*
(Received 23 May 2011; published 29 August 2011)

We study the effect of electron-vibron interactions on the inelastic transport properties of single-molecule nanojunctions. We use the nonequilibrium Green's functions technique and a model Hamiltonian to calculate the effects of second-order diagrams [double-exchange (DX) and dressed-phonon (DPH) diagrams] on the electron-vibration interaction and consider their effects across the full range of parameter space. The DX diagram, corresponding to a vertex correction, introduces an effective dynamical renormalization of the electron-vibron coupling in both the purely inelastic and the inelastic-resonant features of the inelastic electron tunneling spectrum. The purely inelastic features correspond to an applied bias around the energy of a vibron, while the inelastic-resonant features correspond to peaks (resonance) in the conductance. The DPH diagram affects only the inelastic resonant features. We also discuss the circumstances in which the second-order diagrams may be approximated in the study of more complex model systems.

DOI: 10.1103/PhysRevB.84.085433 PACS number(s): 71.38.−k, 73.40.−c, 85.65.+h, 73.63.−b

## I. INTRODUCTION

Junctions consisting of a single organic molecule between two metallic leads hold great promise for future nanoscale devices, where their potential applications include switches, transistors, and sensors. Experimentally, it has proved difficult to control their production in an atomistic manner, and so theoretical studies are crucial for a full understanding of their behavior. It is known that inelastic effects play an important role in the behavior of such devices,[1–10] but as yet we lack a full understanding of the processes at play that will lead to a complete interpretation of experimental results.

In this paper, we use a model-system nanojunction including electron-vibration coupling[11–61] in order to determine, by investigating the whole parameter space, what level of diagrammatic expansion is appropriate to describe the electron-vibration interaction in such junctions. We cover the entire parameter space, thus accounting for all the physical analogs to our model. The parameters we can vary correspond to the lead-molecule-lead coupling, the electron-vibron coupling strength, and the resonance of the electronic level with the leads' electronic states.

In general, an organic molecule-based nanojunction is unlikely to have its highest occupied molecular orbital (HOMO) or lowest unoccupied molecular orbital (LUMO) levels in alignment with the equilibrium Fermi level of the leads, and so such a nanojunction will be dominated by what we term the off-resonant regime with strong tunneling at low bias. Moreover, coupling between the leads and the central molecule is likely to be relatively weak, in the sense that the corresponding coupling to the leads is much smaller than the corresponding hopping integrals in the leads themselves. Conversely, a system consisting of a nanoconstriction in a gold wire will have electronic levels in the constriction that are close to those of the leads, and a larger coupling between the central region and the leads, closer to the tight-binding hopping parameter of the leads.

This paper will distinguish between these regimes and discuss for which physical systems diagrams beyond the self-consistent Born approximation (SCBA) become relevant for electron-phonon coupling. We study this using a full nonequilibrium Green's function (NEGF) technique[11,16,21,23,24,26,27,29–33,38,48,57] which allows us to study all the different transport regimes in the presence of electron-vibron interaction. Following the spirit of many-body perturbation theory and Feynman diagrammatics, we include the commonly used SCBA diagrams as well as second-order diagrams in terms of the electron-vibron interaction. A detailed description of the formalism and the numerical implementation of the NEGF code we have developed is given in Ref. 57. In this work we studied the equilibrium and nonequilibrium electronic structures of the nanojunctions in the presence of electron-vibron coupling. In the present paper, we now give and analyze results for the full nonequilibrium transport properties, namely, the nonlinear $I(V)$ characteristics, the conductance $G(V) = dI/dV$, and especially the IETS signal $d^2I/dV^2$ calculated with our NEGF code.

The paper is structured as follows. In Sec. II we summarize the key aspect of our methodology detailed in Ref. 57. Results for the effects of the second-order diagrams on the nonequilibrium nonlinear transport properties are presented in Sec. III. They are separated into the features we observe for the purely inelastic effects in the inelastic electron tunneling spectrum (IETS) signal at bias equal to an integer multiple of the vibron energy, and for the inelastic resonant features related to the vibron replica of the electronic resonances. Our conclusions are given in Sec. IV. In addition, we explain in detail in the Appendix how one of the second-order diagrams acts as a vertex correction to the Fock-like electron-vibron diagram.

## II. MODEL AND THEORY

A fully atomistic description of the nonequilibrium inelastic transport properties we wish to study is, unfortunately, beyond the reach of current *ab initio* methods. Instead we use a model

 

system which retains the essential physics of the junction while reducing the calculations to a tractable size. A full description of both the model and our methodology is given in Ref. 57, and so we review only the most salient features here.

We use the single-site single-mode model (SSSM), in which the central molecule of the junction is represented by a single molecular level coupled to a single vibrational mode. We have already used this model and discussed its validity in our previous study on the equilibrium and nonequilibrium electronic structures of such a system coupled to two electron reservoirs.[57]

The total Hamiltonian for the nanojunction is given by

$$H_{\text{total}} = H_L + H_R + V_{LC} + V_{CR} + H_C^e + H_{\text{vib}} + H_{e\text{-vib}}. \quad (1)$$

In this work, we represent the Hamiltonian of the left ($L$) and right ($R$) leads $H_{L,R}$ with a noninteracting tight-binding model with semielliptic bands, although in principle it can take any valid form. The hopping between leads and the central region is given by $V_{\alpha C} = t_{0\alpha}(c_\alpha^\dagger d + d^\dagger c_\alpha)$, where $t_{0L,R}$ is the hopping integral between the $\alpha = L, R$ lead and the central region. The central region contains the electron-vibron interactions. We choose that an electron couples linearly, via its density, to the displacement of a single vibration mode. The Hamiltonian for the central region in the SSSM model is then given by

$$\begin{aligned} H_C &= H_C^e + H_{\text{vib}} + H_{e\text{-vib}} \\ &= \varepsilon_0 d^\dagger d + \hbar\omega_0 a^\dagger a + \gamma_0(a^\dagger + a)d^\dagger d, \end{aligned} \quad (2)$$

where $d^\dagger$ ($d$) creates (annihilates) an electron in the molecular level $\varepsilon_0$, which is coupled to the vibration mode of energy $\omega_0$ via the coupling constant $\gamma_0$.

A detailed analysis of the formalism of the nonequilibrium transport properties from NEGF and for an interacting system is provided in Ref. 58. The current $I_\alpha$ passing through each lead $\alpha$ is expressed in terms of two time Green's functions.[62] It is transformed into frequency representation for the steady-state regime to give

$$I_\alpha = \frac{2e}{\hbar}\int \frac{d\omega}{2\pi}\,\text{Tr}\{\Sigma_\alpha^<(\omega)\,G^>(\omega) - \Sigma_\alpha^>(\omega)\,G^<(\omega)\}. \quad (3)$$

We vary the applied bias by moving the chemical potentials of the left and right leads. With the equilibrium Fermi energies $\mu_L^{\text{eq}} = \mu_R^{\text{eq}} = \mu^{\text{eq}} = 0$, we introduce a quantity $\eta_V$ such that $\mu_L = \mu^{\text{eq}} + \eta_V eV$ and $\mu_R = \mu^{\text{eq}} - (1-\eta_V)eV$ following Ref. 63. In this way we can create several forms for the potential drop across the junction. By setting $\eta_V = 1$, for example, we create an asymmetric drop whereby $\mu_R$ remains constant while $\mu_L$ is changed, whereas $\eta_V = 0.5$ gives a symmetric potential drop where $\mu_L$ rises (lowers) as $\mu_R$ lowers (rises) by the same amount.

It now remains to construct our nonequilibrium Green's functions (details given in Ref. 57). The retarded and advanced Green's functions are calculated using a Dyson equation

$$G^{r,a} = g_C^{r,a} + g_C^{r,a}\Sigma^{r,a}G^{r,a}, \quad (4)$$

while the greater ($G^>$) and lesser ($G^<$) Green's functions are obtained from a quantum kinetic equation with the form

$$G^{>,<} = (1 + G^r\Sigma^r)g_C^{>,<}(1 + \Sigma^a G^a) + G^r\Sigma^{>,<}G^a, \quad (5)$$

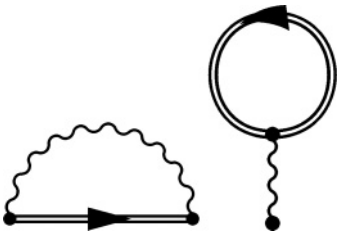

FIG. 1. The Fock-like (F) and Hartree-like (H) diagrams.

where $g_C$ is the *noninteracting* Green's function of the isolated central region.

In this paper we consider both first- and second-order contributions to the electron-vibron coupling. The first-order diagrams are shown in Fig. 1, and, if calculated self-consistently, equate to the commonly used self-consistent Born approximation (SCBA). We also make use of the two second-order diagrams, those which involve two phonon excitations (Fig. 2). The first of these is similar in structure to the $GW$ skeleton for electron-electron interactions, and consists of a Fock-like diagram where the phonon is dressed by a single electron-hole bubble (hence the appellation DPH for dressed-phonon diagram, Fig. 2, left-hand side). The second, which we call the double-exchange (DX) diagram (Fig. 2, right-hand side), includes two phonons simultaneously, with the second being emitted before the first is reabsorbed. The DX diagram is part of the skeleton diagrams corresponding to vertex corrections. We use these diagrams to construct expressions for the electron-vibron self-energy[57] as the (total or partial) sum of each diagram: $\Sigma_{e\text{-vib}}^{\text{total}} = \Sigma_{e\text{-vib}}^{\text{F}} + \Sigma_{e\text{-vib}}^{\text{H}} + \Sigma_{e\text{-vib}}^{\text{DPH}} + \Sigma_{e\text{-vib}}^{\text{DX}}$.

Note that in order to handle numerically sharply peaked functions or strongly discontinuous functions, we have found it necessary to include a very small but finite imaginary part in our expression for the bare vibron Green's function.[57] This also allows us to perform calculations with a smaller number of $\omega$-grid points, as long as our imaginary part $\eta$ in the bare vibron Green's function is approximately two to three times the $\omega$-grid spacing. We have already discussed in detail the effects of the corresponding extra broadening on the line shape of the spectral functions and on the values of the linear conductance in Ref. 57.

## III. RESULTS

In this section we present the effects of the second-order diagrams on the full nonequilibrium transport properties of the nanojunction in the presence of electron-vibron coupling. Calculations of the Green's functions are performed with different levels of approximation for the electron-vibron self-energies (Figs. 1 and 2). Fully self-consistent calculations using the

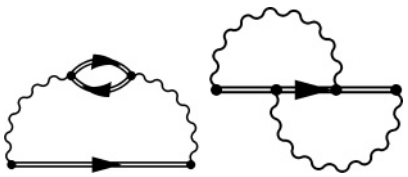

FIG. 2. The dressed-phonon (DPH) and double-exchange (DX) diagrams.

first-order diagrams are annotated SCBA, and those using one or both second-order diagrams are annotated SC(BA + DX), SC(BA + DPH), or SC(BA + DX + DPH) as appropriate. In addition, we have performed non-self-consistent second-order corrections, i.e., by using the SCBA Green's functions to calculate the second-order diagrams, we then determine the different Green's functions without full self-consistency. These calculations are annotated SCBA + DX or SCBA + DPH.

The inelastic properties of the system are present in the current $I(V)$ but are better represented by the second derivative of the current $d^2I/dV^2$ as it is the signal that is directly measured experimentally in the form of the IETS.[1]

The IETS curves present features, peaks, or dips[23,58] at biases corresponding to the energy of a specific excitation, in our case to the energy of one or several excitations of the vibration mode. The peak feature is commonly associated with the opening of a new inelastic channel for the conductance of nanojunctions in the off-resonant regime, i.e., when the electronic level $\varepsilon_0$ is sufficiently far from the equilibrium Fermi level. In the case of the resonant transport regime (when $\varepsilon_0$ is close to $\mu^{\rm eq}$), a dip feature is obtained in the IETS. It is associated with electron-vibron backscattering effects and a decrease in the conductance at the threshold bias. Furthermore, being the derivative of the conductance, the IETS curves also present features at biases corresponding to peaks in the conductance. We have found[57] that in order to get a better aspect ratio for the IETS features corresponding to vibron excitations, it is more convenient to normalize the IETS curves by the dynamical conductance, i.e., $[d^2I/dV^2]/[dI/dV] = d/dV \ln G(V)$ as in Refs. 1,3–5,7,8,10.

We divide our results into two sections: the first for purely inelastic features, and the second for inelastic features associated with the electron resonance effects. The first category corresponds to features observed in the IETS signal at bias equal to an integer multiple of the vibron energy $n\omega_0$, i.e., a tunneling electron excites $n$ vibrons. The second category corresponds to inelastic resonant tunneling via the vibron replica associated with the main electronic resonance at $\tilde{\varepsilon}_0 \sim \varepsilon_0 - \gamma_0^2/\omega_0$, and hence are observed in the IETS signal for biases $V \sim \tilde{\varepsilon}_0 \pm n\omega_0$. We will see below that the second-order diagrams have different effects on the IETS features depending upon their correspondence to one of these two categories.

### A. Purely inelastic features

We consider first of all the off-resonant regime. In this limit the IETS features associated with inelastic resonant tunneling are sufficiently far (or sufficiently small for the higher vibron replica) from the inelastic feature at $V = \omega_0$. We can thus avoid a superposition of the two different kinds of features.

Results are presented in Fig. 3 for different electron-vibron couplings and for both symmetric and asymmetric potential drops. We note that, as would be expected intuitively, the size of the feature increases with the electron-phonon coupling $\gamma_0$—in fact the height with respect to the baseline is proportional to $\gamma_0^2$. As $t_{0L,R}$ is increased, the IETS signal decreases in overall magnitude, although the feature at $\omega_0$ itself remains clear (Fig. 3 inset).

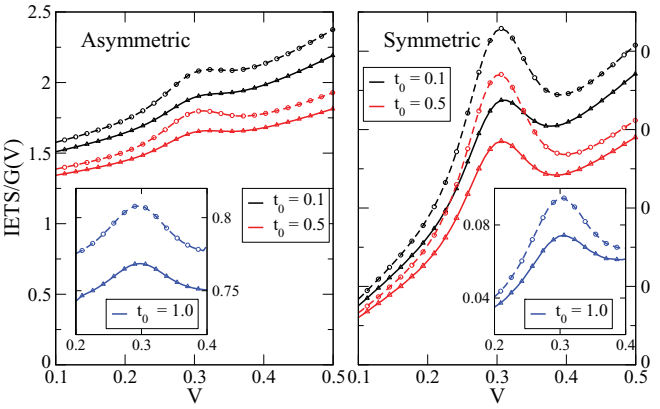


FIG. 3. (Color online) The inelastic peak in the IETS around $V = \omega_0 = 0.3$ for an asymmetric potential drop ($\eta_V = 1.0$, left-hand panel) and a symmetric potential drop ($\eta_V = 0.5$, right-hand panel). Results are shown for three different lead-molecule coupling parameters $t_0 = t_{0L,R}$ (black, red, and blue lines), and for two different electron-vibron couplings (medium $\gamma_0 = 0.195$, solid lines and triangles; strong $\gamma_0 = 0.25$, dashed lines and circles). Lines represent calculations at the SCBA level, symbols SC(BA + DPH), from which we can see there is no distinguishable contribution to the inelastic peak from DPH for any parameter set. The other parameters are $\varepsilon_0 = +1.5$, $\omega_0 = 0.3$, $\eta = 0.030$.

In the off-resonant regime, we do not find any difference to the curves when the second-order DPH diagram is included. Possible reasons for this are discussed in Sec. III B.

We also note that the results are dependent on the symmetry of the potential drops at the left- and right-hand contacts. As shown in the separate panels of Fig. 3, the curves for symmetric potential drops have a much lower baseline than for the asymmetric potential drops, although the inelastic features have the same line shape, position, and magnitude (see Figs. 3, 4, and 7). This is because (for positive bias) in the asymmetric case, $\mu_L$ is rising bias while $\mu_R$ is kept fixed at its equilibrium

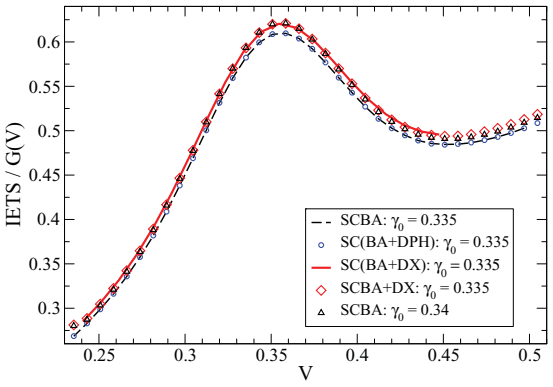


FIG. 4. (Color online) Normalized IETS signal for the inelastic peak at $\omega_0 = 0.35$. Results for SCBA and SC(BA + DPH) are virtually identical. However, including the DX diagram, either self-consistently (solid red line) or non-self-consistently (red diamonds) raises the amplitude of the peak. This effect can be approximated by an SCBA calculation done with a larger $\gamma_0$ (black triangles), indicating that DX generates an effective renormalization of $\gamma_0$. The other parameters are $\varepsilon_0 = +1.5$, $\omega_0 = 0.35$, $t_{0L,R} = 0.10$, $\eta = 0.039$, $\eta_V = 0.5$.

value. Thus $\mu_L$ is approaching the electron resonance twice as fast as in the symmetric case, where $\mu_L$ rises at the same rate as $\mu_R$ falls. The symmetric case therefore contains much less effect from the tail of the main electron resonance, and allows us to further isolate the purely inelastic part of the IETS signal.

We now consider the effect of the double-exchange diagram (Fig. 2, right-hand side) on the inelastic peak at $\omega_0$. Calculation of $\Sigma^{\mathrm{DX}}_{e\text{-vib}}$ is extremely computationally intensive, as it can be reduced neither to a simple convolution product, nor even to a simple double-convolution product.[57] Calculations for the integration in the energy representation of the Green' functions and the self-energies scale as the cube of the number $N_\omega$ of points in the energy grid.[57] Moreover, as the finite imaginary part $\eta$ we have included in the vibron Green's function causes extra broadening, if taken too large it washes out much of the effect of the DX diagram. In order to decrease $\eta$ we need to increase the number of grid points, and thus, even for our minimal model, a fully self-consistent calculation of the double-exchange diagram becomes intractable with $N_\omega > 2000$. Hence for the DX calculations, we usually work with $N_\omega \sim 1500$–$2000$, giving $\eta \sim 0.03$–$0.04$ for the total spectral width considered in our calculations.

We work around this by calculating the effects of the DX diagram both in a self-consistent manner SC(BA + DX) or non-self-consistenly as a second-order correction to the SCBA result.

The results of this are plotted in Fig. 4. We see that the effect of the DX diagram is to both increase the height of the feature and to raise its baseline. For the set of parameters shown the self-consistency in the DX diagram calculations is not crucial.

We see that the effect of DX can also be reproduced with a SCBA calculation in which we increase the value of $\gamma_0$. Therefore, the DX diagram has the effect of renormalizing $\gamma_0$ as it is part of the skeleton family of vertex correction, as shown in Fig. 5. We can thus approximate the effect of the DX diagram in the IETS with a Fock-like diagram with one renormalized vertex $\tilde{\gamma}_0$.

The amplitude of the peak at $\omega_0$, instead of varying as $\gamma_0^2$, therefore now depends on $\tilde{\gamma}_0\gamma_0$, and so we can define an *effective* electron-vibron coupling constant $\bar{\gamma}_0 = \sqrt{\tilde{\gamma}_0\gamma_0}$, with $\bar{\gamma}_0 > \gamma_0$. This allows us to make a more quantitative analysis of $\tilde{\gamma}_0$ by fitting the SCBA + DX curve to a SCBA curve with electron-vibron coupling $\bar{\gamma}_0$, as shown in Fig. 4.

Furthermore, we can study how $\tilde{\gamma}_0$ and $\gamma_0$ are correlated by performing a series of calculations for different values of the parameters $\gamma_0$ and $\omega_0$, and then fitting the SCBA + DX results to those from SCBA calculations. The results of this are shown in Fig. 6, from which we can see that, to a first approximation, the DX diagram consistently raises the


FIG. 5. Second-order double-exchange (DX) diagram reexpression as a vertex correction to the Fock-like diagram, with a renormalized $\gamma_0 \to \tilde{\gamma}_0$ vertex.

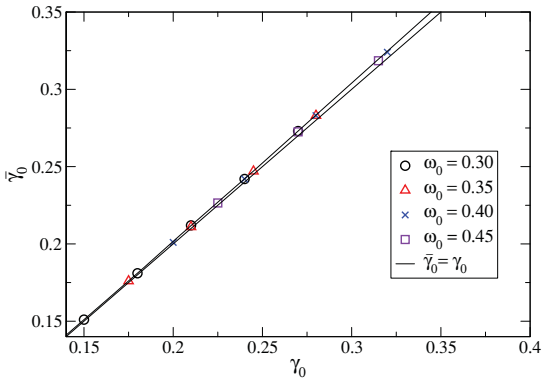


FIG. 6. (Color online) Effective static renormalized electron-vibron coupling parameter $\bar{\gamma}_0$ as a function of the nominal coupling parameter $\gamma_0$, from a fit of several sets of data comparing SCBA + DX curves to SCBA (as in Fig. 4). The data for all three values of $\omega_0$ lie on a straight line with slope 1.03 (the straight line with slope 1 is shown for comparison), implying that the vertex correction increases the effective electron-vibron coupling by 3%.

effective electron-vibron interaction by ∼3% within the range of parameters we used.

However, we would like to point out that although the apparent effects of the DX diagram on the IETS signal is to renormalize the coupling constant $\gamma_0$, the reality is much more subtle. In the Appendix we discuss in detail the renormalization effect of the DX diagram in terms of vertex corrections, and we show that such vertex corrections do not simply correspond to a mapping of the SSSM Hamiltonian onto a similar Hamiltonian with a static renormalization of the electron-vibron coupling constant, i.e., $\gamma_0 \to \bar{\gamma}_0 = \gamma_0 + |\Delta|$. Rather, the vertex correction actually generates a dynamical renormalization of the electron-vibron coupling constant, i.e., $\gamma_0 \to \bar{\gamma}_0(\omega,\omega')$.

This can be seen more clearly by considering SCBA calculations, for different values of the electron-vibron coupling parameter, and checking which of such calculations

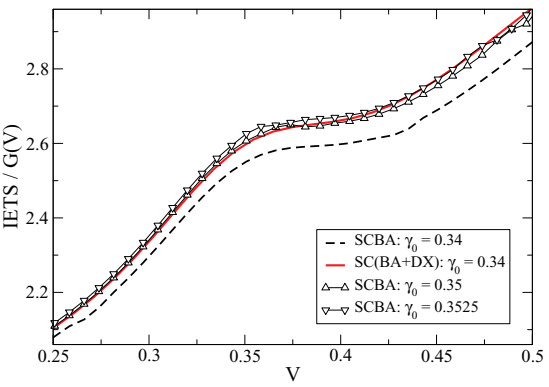


FIG. 7. (Color online) Normalized IETS signal for biases around $\omega_0$ showing different SCBA fits for the renormalized electron-vibron coupling. The SCBA (dashed line) and SC(BA + DX) (solid red line) are shown for $\gamma_0 = 0.34$, together with SCBA calculations for $\gamma_0 = 0.35$ and 0.3525. Although these provide a good approximation, neither gives an exact fit to the line shape of the SC(BA + DX) curve. The other parameters are $\varepsilon_0 = +1.5$, $\gamma_0 = 0.34$, $\omega_0 = 0.35$, $t_{0L,R} = 0.10$, $\eta = 0.039$, $\eta_V = 1.0$.

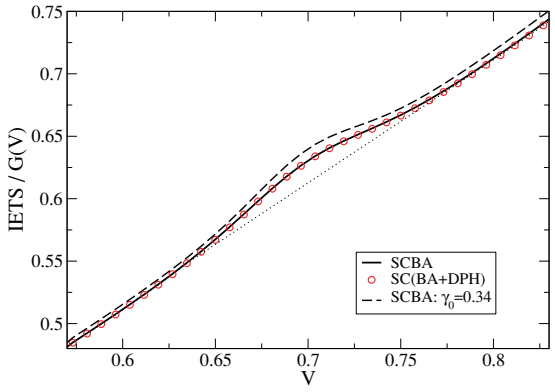


FIG. 8. (Color online) Normalized IETS signal for biases around $2\omega_0$ for different levels of approximation: The SCBA (solid black line) and SC(BA + DPH) (red circles) are virtually identical, as for the feature at $\omega_0$. A SCBA calculation approximating the effect of DX is also included (dashed line). A straight baseline is included for clarity. The other parameters are $\varepsilon_0 = +1.5$, $\gamma_0 = 0.335$, $\omega_0 = 0.35$, $t_{0L,R} = 0.10$, $\eta = 0.009$, $\eta_V = 0.5$.

correspond the best to a SC(BA + DX) calculation. The result is shown in Fig. 7. Although the difference between the best SCBA fits and the SC(BA + DX) are not large, it is quite clear that a renormalized SCBA calculation does not provide exactly the same line shape as a full SC(BA + DX) calculation for all the range of biases $V$ around the inelastic peak at $\omega_0$.

Finally we expect to see a peak feature at $V \sim 2\omega_0$ in the IETS for the off-resonant transport regime. This peak feature is the two-vibration excitation equivalent of the feature observed at $V = \omega_0$. Since this a higher-order process, the amplitude of the feature should be $\gamma_0^2$ times smaller than the feature at $V = \omega_0$. This feature has a rather small amplitude for all the electron-vibron coupling constants we have considered in this paper since $\gamma_0 < 1$. An example of a closeup of the IETS feature at $V \sim 2\omega_0$ is given in Fig. 8. We find that the amplitude of the peak with respect to the linear baseline is indeed approximately $\gamma_0^2 = 0.112$ (one order of magnitude) smaller than the corresponding amplitude of the peak at $V = \omega_0$ (shown in Fig. 4). Once more we find that the effects of the DPH diagram are negligible for this part of the IETS signal. In Fig. 8 we also include the results of a SCBA calculation for a larger coupling $\gamma_0 = 0.34$ which mimics the renormalization effects of the DX diagram as discussion above.

### B. Inelastic resonant features

The main electron-resonance peak occurs at the polaron-shifted value of $\tilde{\varepsilon}_0 \sim \varepsilon_0 - \gamma_0^2/\omega_0$, and consists of a peak-dip feature in the IETS, as it corresponds to a resonant peak feature in the conductance. With no electron-phonon coupling ($\gamma_0 = 0$), the IETS curve has no features other than the one corresponding to the resonant transmission in the conductance at $V = \varepsilon_0$. Once the electron-phonon coupling is turned on, phonon side-band peaks emerge in the spectral function at energies $\omega = \tilde{\varepsilon}_0 \pm n\omega_0$. The $+n\omega_0$ features correspond to phonon emission (vibration excitation) by an electron, while the $-n\omega_0$ features correspond to phonon-emission by a hole. In the IETS, they appear as peak-dip features (derivatives of an inelastic resonant peak in the conductance) with amplitude

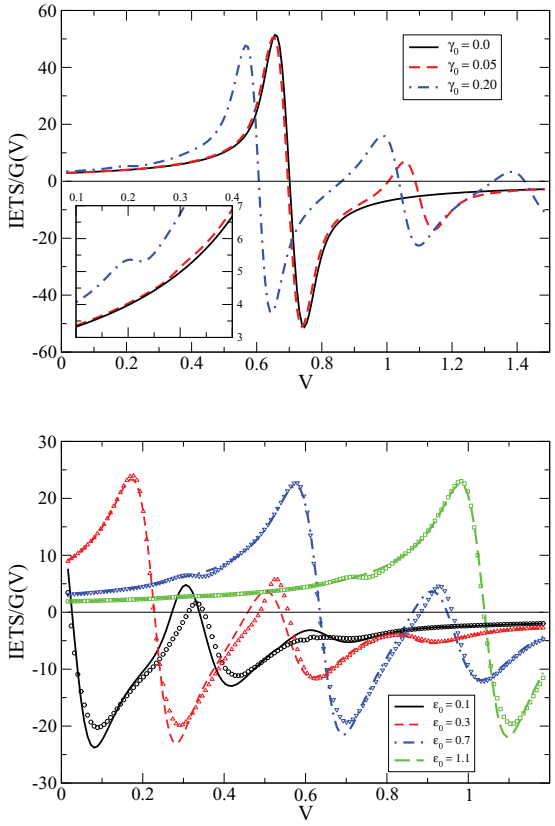


FIG. 9. (Color online) Normalized IETS signal. Top: Inelastic resonant features for different values of $\gamma_0$. With no electron-vibron coupling (solid black line), there is a single feature at $\varepsilon_0 = 0.7$. With electron-vibron coupling (red and blue dashed lines), the main peak moves to $\tilde{\varepsilon}_0 \sim \varepsilon_0 - \gamma_0^2/\omega_0$ and side-band peaks appear. The inset shows a tiny feature at $\tilde{\varepsilon}_0 - \omega_0$ that only occurs for $t_0 \lesssim 0.1$ in SCBA calculations but reappears for all $t_0$ once DPH is included. Bottom: The inelastic resonant features for various $\varepsilon_0$ at $\gamma_0 = 0.15$ for both SCBA (lines) and SC(BA + DPH) (symbols) calculations, showing the increasing influence of DPH in the resonant transport regime $\varepsilon_0 \to 0$. The other parameters are $t_0 = 0.2$, $\omega_0 = 0.3$, $\eta_V = 1.0$, $\eta = 0.03$.

decreasing as the bias is further increased. At lower biases, however, there are no features at $\omega = \tilde{\varepsilon}_0 - n\omega_0$ at the SCBA level except for very low values of the coupling to the leads ($t_{0L,R} \lesssim 0.1$, Fig. 9, top inset).

Including the DPH diagram, however, introduces a small peak-dip features at $\tilde{\varepsilon}_0 - \omega_0$ just below the main peak-dip feature at $V \sim \tilde{\varepsilon}_0$ in the IETS, as shown in Fig. 9. The DPH diagram also has a strong influence on the line shape of the other phonon side-band peaks above $\tilde{\varepsilon}_0$, increasingly so as $\varepsilon_0$ is brought within range of the equilibrium chemical potentials (i.e., $\tilde{\varepsilon}_0 \to 0$ in Fig. 9, bottom).

We now consider the combined effects of the DPH diagram as well as of the DX diagram on the specific case of the IETS feature at $\tilde{\varepsilon}_0 - \omega_0$. This is shown in Fig. 10. The DPH diagram increases strongly the peak-dip feature (at $V \sim \tilde{\varepsilon}_0 - \omega_0$) obtained from SCBA calculations at medium and strong electron-vibron coupling. Note here the importance of the self-consistency in the calculations: The second-order DPH diagram calculated as a second-order correction to SCBA

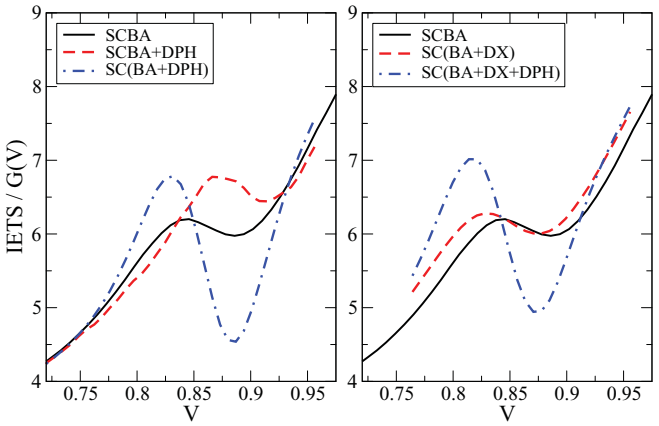


FIG. 10. (Color online) Normalized IETS signal for biases around the first vibration side-band peak $V \sim \tilde{\varepsilon}_0 - \omega_0 = 1.19$–$0.4 \sim 0.8$. Calculations performed for different approximations for the electron-vibron self-energy: (Left-hand panel) SCBA (black solid line), SCBA plus second-order DPH correction (dashed red line), and SC(BA + DPH) (dotted-dashed blue line); (right-hand panel): SCBA (solid black line), SC(BA + DX) (dashed red line), and SC(BA + DX + DPH) (dotted-dashed blue line). The other parameters are $\varepsilon_0 = +1.5$, $\gamma_0 = 0.35$, $\omega_0 = 0.4$, $t_{0L,R} = 0.09$, $\eta = 0.039$, $\eta_V = 1$.

(Fig. 10, left-hand side) gives a completely wrong feature in the IETS.

Interestingly, the self-consistent calculation with the DX diagram seems to give a similar feature to that observed in the SCBA calculations, but slightly shifted toward lower bias (Fig. 10, right-hand side). This is completely consistent with the renormalization effects of the electron-vibron coupling by the DX diagram as discussed in the previous section. Indeed, the DX diagram renormalizes the coupling $\gamma_0$ toward a higher value $\bar{\gamma}_0$. Consequently the renormalization of the molecular level by $-\bar{\gamma}_0^2/\omega_0$ is more important than for SCBA calculations, and thus the feature is moved toward lower bias.

The calculations performed with both DX and DPH diagrams (Fig. 10, right-hand side) generate a hybrid feature in the IETS in comparison to individual calculations with the second-order diagrams. However, the new IETS is not simply obtained by a linear superposition of the individual effects of the DPH and DX diagrams.

It might at first seem strange that the DPH self-energy is negligible at $V = n\omega_0$, where one might expect it to be influential, but that it has a significant effect at biases $\gtrsim \tilde{\varepsilon}_0$. While this is to some extent related to the strength of the electron-vibron coupling, there is another, more important, underlying cause. The DPH diagram involves an electron-hole bubble, and so for this diagram to become relevant, simultaneous electron and hole states must be available. This is not the case when the spectral functions of the coupled electron-vibron system are mostly empty or mostly filled. When the bias is significantly low and both Fermi levels $\mu_{L,R}$ are below the electron resonance level, these excitations are inaccessible and so there are no effects from the DPH diagram. Once the bias is increased to within range of $\tilde{\varepsilon}_0$, or $\tilde{\varepsilon}_0 \pm n\omega_0$, however, these electron-hole states become accessible and the

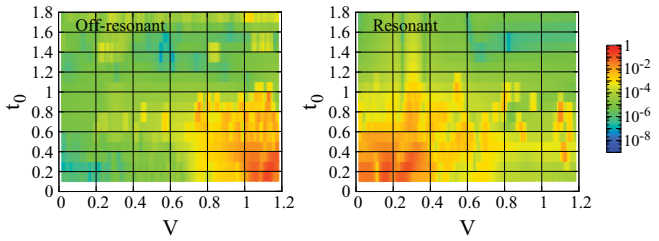


FIG. 11. (Color online) Maps generated from multiple calculations of SCBA and SC(DA + DPH) IET spectra for the off-resonant (left-hand panel) and resonant (right-hand panel) regimes showing the normalized absolute ratio of the SCBA and SC(BA + DPH) spectra $|1 - \frac{\mathrm{IETS}_{\mathrm{SC(BA+DPH)}}}{\mathrm{IETS}_{\mathrm{SCBA}}}|$. It gives a near-zero result (blue and green areas) when the two calculations give the same spectrum, and a positive number [red areas, i.e., bottom right-hand corner for SCBA and bottom left-hand corner for SC(BA + DPH)] where there is a substantial difference between the two. The other parameters are $\varepsilon_0 = 1.5/0.0$ (off-resonant/resonant), $\gamma_0 = 0.195$, $\omega_0 = 0.3$.

DPH diagram becomes influential (unless the spectral function is mostly filled). This is also borne out by the increasing contribution from DPH to the line shape of the phonon side-band peaks as the electron level $\varepsilon_0$ is decreased, moving DPH's sphere of influence to lower and lower biases (see the lower panel in Fig. 9).

### C. Summary over the entire parameter range

Having examined the role of the second-order diagrams in detail for characteristic selected sets of parameters, we now show results across the entire parameter range. In order to present this in a concise manner, we have compiled maps of our IETS results comparing SCBA calculations to those with SC(BA + DPH), indicating in which regimes the DPH self-energy has a significant effect. For the off-resonant regime (Fig. 11, left-hand side), we can see that the greatest effect of DPH is apparent at higher bias (i.e., approaching the electron resonance $\varepsilon_0$) and when the lead-molecule-lead coupling is small. For the resonant case, however, we can see that the DPH self-energy only gives a non-negligible contribution in the region of parameter space where the coupling to the leads is small, and at low bias.

This has potential implications for real molecular junctions. Consider a junction which has its dominant molecular levels far from the equilibrium Fermi levels of the leads. At sufficiently high bias, the DPH self-energy will have a significant contribution to the inelastic spectra. This could occur in the case of a junction formed from an organic molecule if the electronic level of the molecule is within range of the intended operational bias of the junction. If, however, the dominant molecular electronic level is close to the leads' Fermi levels, and the coupling to the leads is large (as would be the case, for example, in a gold nanoconstriction) then DPH will not give a significant contribution at any applied bias.

## IV. CONCLUSIONS

By using the nonequilibrium Green's functions technique, we have studied the effect of electron-vibron interaction on

the inelastic transport properties of single-molecule nanojunctions for a model system. We have included not only the first-order diagrams (BA) but also the second-order diagrams [double-exchange (DX) and dressed-phonon (DPH) diagrams] for the electron-vibration interaction. We have calculated the inelastic electron tunneling spectrum (IETS) across the full range of parameters available to our model. The effects of the second-order DX and DPH diagrams are different and affect different features of the IETS signal. The effects of these diagrams are generally less visible in the integrated quantities, such as the current or the derivated IETS signal, than in the spectral functions.[57] However, their effects are non-negligible, and are important for the full understanding of the spectroscopic information conveyed by the IETS signal.

The effect of the dressed-phonon (DPH) diagram is more important in the bias regions where one of the leads' chemical potentials begins to impinge upon the electron resonance or one of its vibron replica (i.e., for resonant inelastic features). Its effect is reduced both by increasing the lead-molecule-lead coupling and/or reducing the electron-vibron interaction. The renormalization of the vibron propagator (DPH) has been shown to be strongly dependent on the self-consistency of the calculations. It would be interesting now to study the effects of the full series of the electron-hole bubble on the renormalized vibron propagator (i.e., full $GW$-like diagram).

The double-exchange diagram (DX) affects all the features in the IETS signal (i.e., resonant inelastic features and purely inelastic features at $V \sim \omega_0$). The corrections are small in the weak-to-medium electron-vibron coupling because they are of the order of $O(\gamma_0^4)$. However, we have shown, numerically and analytically, that the effect of DX is similar to a dynamical renormalization of one vertex in the Fock-like diagram. More interestingly, the complex form of the nonequilibrium dynamical renormalized electron-vibron coupling $\tilde{\gamma}_0(\omega,\omega')$ we have derived analytically can be adequately replaced in our IETS calculations by a single static renormalized parameter $\bar{\gamma}_0$. This important result leads us to believe that the second-order DX calculations, which are extremely costly in computing time even for our model system, can be incorporated in calculations for realistic systems by an appropriate renormalization of the vertex in a low-computing-cost SCBA calculation.

## ACKNOWLEDGMENT

This work was funded in part by the European Community's Seventh Framework Programme (FP7/2007-2013) under Grant agreement No. 211956 (ETSF e-I3 grant).

## APPENDIX: NONEQUILIBRIUM VERTEX CORRECTIONS TO THE FOCK DIAGRAM

In Appendix A of Ref. 57 we have given all the details for the derivations of the first- and second-order electron-vibron self-energies. In this Appendix we show how the second-order double-exchange (DX) diagram can be recast in an effective first-order Fock-like diagram with a renormalized vertex.

We recall that for the SSSM model, the Fock and DX self-energies defined on the Keldysh contour $C_K$ are given by

$$\Sigma^{F}_{e\text{-vib}}(\tau_1,\tau_2) = \mathrm{i}\gamma_0^2\, D_0(\tau_1,\tau_2)\, G(\tau_1,\tau_2) \tag{A1}$$

and

$$\Sigma^{DX}_{e\text{-vib}}(\tau_1,\tau_2) = -\frac{\gamma_0^4}{3}\int_{C_K} d\tau_3\, d\tau_4\, G(\tau_1,\tau_3)D_0(\tau_1,\tau_4) \times G(\tau_3,\tau_4)D_0(\tau_3,\tau_2)G(\tau_4,\tau_2). \tag{A2}$$

The DX self-energy can be rewritten as an effective Fock-like diagram after introducing a renormalized electron-vibron coupling parameter $\tilde{\gamma}_0(\tau_3,\tau_4;\tau_2)$ and the vertex function $\Gamma(\tau_3,\tau_4;\tau_2)$:

$$\Sigma^{DX}_{e\text{-vib}}(\tau_1,\tau_2) = i\gamma_0\int_{C_K} d\tau_3\, d\tau_4\, \tilde{\gamma}_0(\tau_3,\tau_4;\tau_2) \times D_0(\tau_1,\tau_4)G(\tau_1,\tau_3), \tag{A3}$$

with

$$\tilde{\gamma}_0(\tau_3,\tau_4;\tau_2) = \frac{i\gamma_0^3}{3}\Gamma(\tau_3,\tau_4;\tau_2), \tag{A4}$$

and where the vertex function is given by

$$\Gamma(\tau_3,\tau_4;\tau_2) = G(\tau_3,\tau_4)D_0(\tau_3,\tau_2)G(\tau_4,\tau_2). \tag{A5}$$

The above expression for the vertex function is compatible with the second-order expansion of the electron-vibron interaction. A generalization of the vertex function (see the Fock-like diagram in Fig. 5) to all orders of the interaction is possible, though beyond the scope of the present paper. Note that at the lowest order, the renormalized electron-vibron coupling parameter would be given by $\tilde{\gamma}_0(\tau_3,\tau_4;\tau_2) = \gamma_0\Gamma^{(0)}(\tau_3,\tau_4;\tau_2)$ with $\Gamma^{(0)}(\tau_3,\tau_4;\tau_2) = \delta(\tau_3-\tau_2)\delta(\tau_4-\tau_2)$. Hence Eq. (A2) would simply be transformed Eq. (A1) as expected.

Using the rules of analytical continuation on the real-time branches given in Appendix A of Ref. 57, we find the different components of the self-energies. Then after taking the Fourier transform of the different quantities in the steady-state limit, i.e., $X(t,t') = X(t-t')$, we find the following expression for the different components of the energy-dependent self-energies:

$$\Sigma^{F,\zeta_1\zeta_2}_{e\text{-vib}}(\omega) = i\gamma_0^2\int\frac{dv}{2\pi}G^{\zeta_1\zeta_2}(v)D_0^{\zeta_1\zeta_2}(\omega-v) \tag{A6}$$

and

$$\Sigma^{DX,\zeta_1\zeta_2}_{e\text{-vib}}(\omega) = i\gamma_0\int\frac{dv}{2\pi}\sum_{\zeta_3,\zeta_4}\zeta_3\zeta_4 G^{\zeta_1\zeta_3}(v)D_0^{\zeta_1\zeta_4}(\omega-v) \times\tilde{\gamma}_0^{\zeta_3\zeta_4\zeta_2}(\omega,v), \tag{A7}$$

where the nonequilibrium dynamical renormalized electron-vibron coupling is given by

$$\tilde{\gamma}_0^{\zeta_3\zeta_4\zeta_2}(\omega,v) = \frac{i\gamma_0^3}{3}\int\frac{du}{2\pi}G^{\zeta_3\zeta_4}(v-u) \times D_0^{\zeta_3\zeta_2}(u)G^{\zeta_4\zeta_2}(\omega-u). \tag{A8}$$

[The index $\zeta_i = \pm$ labels the branch of the Keldysh time-loop contour $C_K$ and are related to the usual convention: time-ordered ($t = ++$), anti-time-ordered ($\tilde{t} = --$), greater ($>= -+$), and lesser ($<= +-$) components.]

Because all the quantities are originally defined on $C_K$ and because the vertex function is a three-point (three times) function, the nonequilibrium dynamical renormalized electron-vibron coupling is a complex function of three indices $\zeta_i$ and of two energy variables. Such a dynamical renormalization (including nonequilibrium conditions) is much more complicated than a simple static renormalization of the electron-vibron constant coupling $\gamma_0 \rightarrow \tilde{\gamma}_0$.

In our analysis of the IETS signal in the off-resonant transport regime, we try to keep the interpretation of the results as simple as possible, and we show that the renormalization of the IETS signal due to the DX diagram can be fairly well approximated by a simple static renormalization of the coupling constant $\gamma_0$ for applied bias around the vibration frequency $V \sim \omega_0 \pm 20\%$.

*louise.dash@york.ac.uk


[1] K. W. Hipps and U. Mazur, J. Phys. Chem. **97**, 7803 (1993).
[2] N. Liu, N. A. Pradhan, and W. Ho, J. Chem. Phys. **120**, 11371 (2004).
[3] J. G. Kushmerick, J. Lazorcik, C. H. Patterson, and R. Shashidhar, Nano Lett. **4**, 639 (2004).
[4] L. H. Yu, Z. K. Keane, J. W. Ciszek, L. Cheng, M. P. Stewart, J. M. Tour, and D. Natelson, Phys. Rev. Lett. **93**, 266802 (2004).
[5] L. H. Yu, C. D. Zangmeister, and J. G. Kushmerick, Nano Lett. **6**, 2515 (2006).
[6] D.-H. Chae, J. F. Berry, S. Jung, F. A. Cotton, C. A. Murillo, and Z. Yao, Nano Lett. **6**, 165 (2006).
[7] J. M. Beebe, H. J. Moore, T. R. Lee, and J. G. Kushmerick, Nano Lett. **7**, 1364 (2007).
[8] N. Okabayashi, Y. Konda, and T. Komeda, Phys. Rev. Lett. **100**, 217801 (2008).
[9] H. Gawronski, J. Fransson, and K. Morgenstern, Nano letters **11**, 2720 (2011).
[10] Y. Kim, H. Song, F. Strigl, H.-F. Pernau, T. Lee, and E. Scheer, Phys. Rev. Lett. **106**, 196804 (2011).
[11] P. Hyldgaard, S. Hershfield, J. H. Davies, and J. W. Wilkins, Ann. Phys. **236**, 1 (1994).
[12] H. Ness and A. J. Fisher, Phys. Rev. Lett. **83**, 452 (1999).
[13] H. Ness, S. A. Shevlin, and A. J. Fisher, Phys. Rev. B **63**, 125422 (2001).
[14] H. Ness and A. J. Fisher, Europhys. Lett. **57**, 885 (2002).
[15] K. Flensberg, Phys. Rev. B **68**, 205323 (2003).
[16] T. Mii, S. Tikhodeev, and H. Ueba, Phys. Rev. B **68**, 205406 (2003).
[17] M. J. Montgomery, J. Hoekstra, A. P. Sutton, and T. N. Todorov, J. Phys. Condens. Matter **15**, 731 (2003).
[18] A. Troisi, M. A. Ratner, and A. Nitzan, J. Chem. Phys. **118**, 6072 (2003).
[19] Y. C. Chen, M. Zwolak, and M. di Ventra, Nano Lett. **4**, 1709 (2005).
[20] N. Lorente and M. Persson, Phys. Rev. Lett. **85**, 2997 (2000).
[21] T. Frederiksen, M. Brandbyge, N. Lorente, and A. P. Jauho, Phys. Rev. Lett. **93**, 256601 (2004).
[22] M. Galperin, M. A. Ratner, and A. Nitzan, Nano Lett. **4**, 1605 (2004).
[23] M. Galperin, M. A. Ratner, and A. Nitzan, J. Chem. Phys. **121**, 11965 (2004).
[24] A. Mitra, I. Aleiner, and A. J. Millis, Phys. Rev. B **69**, 245302 (2004).
[25] A. Pecchia, A. Di Carlo, A. Gagliardi, S. Sanna, T. Frauenhein, and R. Gutierrez, Nano Lett. **4**, 2109 (2004).
[26] A. Pecchia and A. Di Carlo, Rep. Prog. Phys. **67**, 1497 (2004).
[27] Z. Chen, R. Lü, and B. Zhu, Phys. Rev. B **71**, 165324 (2005).
[28] M. Paulsson, T. Frederiksen, and M. Brandbyge, Phys. Rev. B **72**, 201101 (2005).
[29] D. A. Ryndyk and J. Keller, Phys. Rev. B **71**, 073305 (2005).
[30] N. Sergueev, D. Roubtsov, and H. Guo, Phys. Rev. Lett. **95**, 146803 (2005).
[31] J. K. Viljas, J. C. Cuevas, F. Pauly, and M. Häfner, Phys. Rev. B **72**, 245415 (2005).
[32] T. Yamamoto, K. Watanabe, and S. Watanabe, Phys. Rev. Lett. **95**, 065501 (2005).
[33] A. Cresti, G. Grosso, and G. P. Parravicini, J. Phys. Condens. Matter **18**, 10059 (2006).
[34] M. Kula, J. Jiang, and Y. Luo, Nano Lett. **6**, 1693 (2006).
[35] M. Paulsson, T. Frederiksen, and M. Brandbyge, Nano Lett. **6**, 258 (2006).
[36] D. A. Ryndyk, M. Hartung, and G. Cuniberti, Phys. Rev. B **73**, 045420 (2006).
[37] A. Troisi and M. A. Ratner, Nano Lett. **6**, 1784 (2006).
[38] L. de la Vega, A. Martín-Rodero, N. Agraït, and A. Levy-Yeyati, Phys. Rev. B **73**, 075428 (2006).
[39] M. C. Toroker and U. Peskin, J. Chem. Phys. **127**, 154706 (2007).
[40] T. Frederiksen, M. Paulsson, M. Brandbyge, and A.-P. Jauho, Phys. Rev. B **75**, 205413 (2007).
[41] M. Galperin, A. Nitzan, and M. A. Ratner, Phys. Rev. B **74**, 075326 (2007).
[42] D. A. Ryndyk and G. Cuniberti, Phys. Rev. B **76**, 155430 (2007).
[43] B. B. Schmidt, M. H. Hettler, and G. Schön, Phys. Rev. B **75**, 115125 (2007).
[44] A. Troisi, J. M. Beebe, L. B. Picraux, R. D. van Zee, D. R. Stewart, M. A. Ratner, and J. G. Kushmerick, Proc. Natl. Acad. Sci. USA **104**, 14255 (2007).
[45] Y. Asai, Phys. Rev. B **78**, 045434 (2008).
[46] C. Benesch, M. Čížek, J. Klimeš, I. Kondov, M. Thoss, and W. Domcke, J. Phys. Chem. C **112**, 9880 (2008).
[47] M. Paulsson, T. Frederiksen, H. Ueba, N. Lorente, and M. Brandbyge, Phys. Rev. Lett. **100**, 226604 (2008).
[48] R. Egger and A. O. Gogolin, Phys. Rev. B **77**, 113405 (2008).
[49] S. Monturet and N. Lorente, Phys. Rev. B **78**, 035445 (2008).
[50] E. J. McEniry, T. Frederiksen, T. N. Todorov, D. Dundas, and A. P. Horsfield, Phys. Rev. B **78**, 035446 (2008).
[51] D. A. Ryndyk, R. Gutirrez, B. Song, and G. Cuniberti, in *Energy Transfer Dynamics in Biomaterial Systems*, edited by I. Burghardt, V. May, D. A. Micha, and E. R. Bittner, Springer Series in Chemical Physics (Springer, Berlin, 2009) Vol. 93, pp. 213–335.

[52]B. B. Schmidt, M. H. Hettler, and G. Schön, Phys. Rev. B **77**, 165337 (2008).
[53]M. Tsukada and K. Mitsutake, J. Phys. Soc. Jpn. **78**, 084701 (2009).
[54]J. Loos, T. Koch, A. Alvermann, A. R. Bishop, and H. Fehske, J. Phys. Condens. Matter **21**, 395601 (2009).
[55]R. Avriller and A. L. Yeyati, Phys. Rev. B **80**, 041309 (2009).
[56]F. Haupt, T. Novotný, and W. Belzig, Phys. Rev. Lett. **103**, 136601 (2009).
[57]L. K. Dash, H. Ness, and R. W. Godby, J. Chem. Phys. **132**, 104113 (2010).
[58]H. Ness, L. Dash, and R. W. Godby, Phys. Rev. B **82**, 085426 (2010).
[59]H. Wang and M. Thoss, e-print arXiv:1103.4945v1.
[60]A. Garcia-Lekue, D. Sanchez-Portal, A. Arnau, and T. Frederiksen, e-print arXiv:1103.4302v1.
[61]A. Ueda, O. Entin-Wohlman, and A. Aharony, e-print arXiv:1101.4440v1.
[62]Y. Meir and N. S. Wingreen, Phys. Rev. Lett. **68**, 2512 (1992).
[63]S. Datta, W. D. Tian, S. H. Hong, R. Reifenberger, J. I. Henderson, and C. P. Kubiak, Phys. Rev. Lett. **79**, 2530 (1997).